European Journal of Mechanics / B Fluids 76 (2019) 413–421

Contents lists available at ScienceDirect

European Journal of Mechanics / B Fluids

journal homepage: www.elsevier.com/locate/ejmflu

Instability of isolated boundary-layer streaks to spatially-developing travelling waves

R.E. Hewitt *, P.W. Duck

School of Mathematics, University of Manchester, UK

ARTICLE INFO

Article history:
Received 17 December 2018
Received in revised form 11 April 2019
Accepted 16 April 2019
Available online 24 April 2019

Keywords:
Boundary layer
Stability
Transition
Streaks

ABSTRACT

The spatial stability properties of an isolated low-speed streak embedded in a Blasius boundary layer are determined; the streak is generated by steady localised injection, whilst the disturbance is generated by a linear harmonic localised injection. Isolated streaks driven by short-scale spanwise forcing have comparable growth rates of both sinuous and varicose instabilities. These features have been discussed previously via DNS methods, but the novel aspect here is a treatment via a rationally-parabolised version of the Navier–Stokes equations in the high Reynolds number limit. The parabolic formulation allows for a more efficient and Reynolds number independent computation of fully three-dimensional non-parallel streaks their stability. We compute the non-parallel development of a perturbation by downstream marching from a time-harmonic disturbance generator (in tandem with the streamwise streak development), before comparing these results with bi-global eigenvalue calculations. The stability properties are well captured by a weakly non-parallel eigenvalue formulation of the boundary-region equations, provided that one is not in the vicinity of the disturbance generator. Further downstream, or at higher excitation frequencies we directly recover the long-wave limit of a two-dimensional Rayleigh stability problem. Even further downstream (or at even higher excitation frequencies, which is mathematically equivalent) we must return to a (two-dimensional) Rayleigh formulation as the streamwise wavelength of the disturbance becomes comparable to the boundary-layer thickness. For streaks that are comparable with those obtained experimentally our spatial growth rates and eigenmode shapes compare favourably with the experimentally-determined values. For the range of streaks considered, we demonstrate the sinuous mode retains the higher growth rate in the viscous stability problem. The experimentally-observed change over to a dominant varicose mode nearer the disturbance site is shown to be true only for frequencies that provoke an inviscid response.

1. Introduction and formulation

Localised surface roughness is known to have a substantial impact on the route of laminar–turbulent transition in boundary-layer flows, and there are a number of experimental/numerical studies that examine the stability of flow over a three-dimensional roughness element. These surface-mounted roughness elements are typically cylindrical [1,2], hemispherical [3,4], conical [5], rectangular cuboid [6], mesh screens [7] or (smooth) bumps [8], and placed on otherwise flat plate in a uniform free stream. As a consequence of the presence of the roughness element, in the 'wake' there develops streamwise-aligned vortices with associated streamwise streaks. Whilst streaks tend to be more prominent for sharp-sided roughness elements, the generic features of the streaks are consistent across a range of disturbance generators, not limited to just surface roughness, but also including (for example) surface injection over the same length scales. This is to be expected at least in the far downstream limit, because the recent work of [9] has demonstrated that a downstream-decaying streak in a Blasius boundary layer can be described (in this linearised regime) in terms of algebraic, steady, localised, self-similar, bi-global eigenmodes.

For carefully chosen distributions of three-dimensional surface roughness it is possible to stabilise the two-dimensional Tollmien–Schlichting mechanism [10,11] and for similar scale surface injection (in the presence of a free stream pressure gradient) it is possible to prevent separation [12]. However in all cases, as the height of the surface roughness (or strength of the surface injection) is increased, the streak that is induced downstream of the disturbance region ultimately becomes unstable, leading to transition.

The problem of determining the stability of streaks has been tackled via a range of approaches, for example, experimentally [7], numerically via global stability analyses and DNS [1,13], as well

* Corresponding author.
E-mail address: richard.hewitt@manchester.ac.uk (R.E. Hewitt).

https://doi.org/10.1016/j.euromechflu.2019.04.011
0997-7546/

as local parallel theories [14], global optimal perturbations [15] and in compressible flow through bi-global eigenvalue computations and three-dimensional PSE analyses [6]. In some cases the analysis points to sinuous modes dominating the response, whilst in others varicose modes are suggested to be the most relevant. Furthermore, even in sub-critical cases where varicose and sinuous modes are both stable, optimal perturbations can still achieve large growth [2]. In [1] both sinuous and varicose modes have been located as global eigenmodes for flow past (circular) cylindrical roughness elements, with the aspect ratio of the cylinder playing a major role in the selection of the dominant mode.

An approach that has not been considered in as much detail (and which we pursue herein) is one based on the assumption of an asymptotically large Reynolds number. This methodology has a substantial simplifying advantage of formally reducing the governing equations of both the base flow and perturbation to being parabolic systems. To pursue this approach we consider incompressible flow over a semi-infinite flat plate, which in the absence of any additional forcing merely results in the classical two-dimensional Blasius solution. However, our focus here lies in the spatially developing instability of a single streak structure embedded in this Blasius flow, as induced by a spatially localised boundary injection. This localised injection could equally be an isolated roughness element, but one that is elongated in the streamwise direction to match the required boundary-layer scales. The resulting elongated streaks are $O(Re^{-1/2}) \times O(Re^{-1/2})$ in the (dimensionless) cross-sectional plane in the high Reynolds number ($Re \gg 1$) limit. As such, any high Reynolds number reduction must retain both transverse *and* spanwise diffusion, therefore only diffusion and pressure gradients in the downstream direction are neglected in this approach.

Investigations that focus on the ($Re \gg 1$) stability of a single streak structure are less common than those that assume periodicity in the spanwise direction. These isolated longitudinal streaks are more challenging in that the flow components in the cross-sectional plane decay towards the free stream only algebraically as shown in [16] (although the corresponding vorticity and streamwise components still decay exponentially). This algebraic behaviour is not found in two-dimensional or classical three-dimensional boundary layers (see for example [17, 18]) and computational formulations that do not capture the far field correctly can be strongly affected by domain truncation. Having obtained a spatially-developing steady streak base flow, any linear stability problem can be approached via the same formulation, although any local eigenvalue analysis is then best formulated as a bi-global problem.

As noted in the context of roughness elements above, isolated low-speed streaks are interesting in that, for sufficiently small spanwise scales, the sinuous and varicose instabilities have been shown to have comparable growth rates. This has been demonstrated both experimentally by Asai et al. [7] and in the corresponding DNS results of Brandt [13]. Motivated by the experimental work reported in [7], the subsequent work of Brandt [13] used a fully three-dimensional, unsteady, spectral formulation of the Navier–Stokes system. The experimental arrangement of [7] employed a mesh screen attached to a flat plate in a uniform flow, to generate a steady streak. This mesh disturbance was modelled in [13] as a volumetric forcing of the streamwise momentum equation with parameters chosen to (approximately) reproduce the steady streak data. To assess the stability of this streak the linearised Navier–Stokes equations were time marched from an impulse response. The later stage nonlinear breakdown of unstable sinuous/varicose perturbations induced by time-harmonic boundary forcing was also considered in [13].

The results of Brandt effectively reproduce the experimental behaviour found by Asai et al. [7] but at substantial computational cost. Our goal here is to show that the same features can be produced by a self-consistent high Reynolds number asymptotic theory based around the 'boundary-region equations'. We focus particularly on [7,13] because a mesh screen 'roughness' has been shown not to lead to reverse flow in the immediate wake, and so seems the most likely candidate for an application of the high-Reynolds number theory.

This general type of 'boundary-region' formulation has been previously employed in (for example) discussions of isolated streaks [16,19,20], spanwise-periodic streaks/vortices [21,22], their transient growth [23–25] and their self-sustained interaction with travelling waves [26].

In terms of a dimensional coordinate system (x^*, y^*, z^*) aligned with the leading edge ($x^* = 0$), we non-dimensionalise with an arbitrary lengthscale L^* in the usual way via

$$x^* = L^* x\,, \quad (y^*, z^*) = L^* Re^{-\frac{1}{2}} (2x)^{\frac{1}{2}} (\eta, \zeta)\,, \tag{1}$$

where $Re = U^*_\infty L^*/\nu^* \gg 1$ is a Reynolds number based on a (uniform) freestream speed U^*_∞ and kinematic viscosity ν^*. In (1) the factor of $(2x)^{1/2}$ is a convenient method of capturing the downstream thickening/broadening of the viscous layer but the solutions we consider have no self-similarity constraint. To allow a later formulation of the linear stability problem for time-harmonic perturbations, we retain the unsteady terms with a corresponding choice for the natural timescale of $t^* = tL^*/U^*_\infty$ (this in itself precludes a self similar response).

The dimensional velocity field (u^*, v^*, w^*) is expanded in the usual manner

$$u^* = U^*_\infty U + \cdots\,, \quad (v^*, w^*) = U^*_\infty Re^{-\frac{1}{2}} (2x)^{-\frac{1}{2}} (V, W) + \cdots\,, \tag{2a}$$

where, in general, U, V, W are functions of x, ζ, η, t. The corresponding pressure field is

$$p^* = \rho^* U^{*2}_\infty \left(Re^{-1/2} p(x,t) + Re^{-1} P(x, \zeta, \eta, t) \right) + \cdots\,, \tag{2b}$$

in the absence of any freestream pressure gradient, with ρ^* the constant density. Here p is a displacement induced correction to the pressure field that does not affect the leading-order system, whilst P must be retained in the leading-order momentum equations in the high Reynolds number limit.

The leading-order system for large Re provides a primitive variable formulation of the 'boundary-region equations', however in what follows we pursue an alternative formulation that arises from a cross differentiation of the momentum equations to usefully eliminate the pressure correction P, following previous authors, including [9]. On a further substitution of

$$(V, W) = (\eta U - \Phi, \zeta U - \Psi)\,, \tag{3}$$

we recover the dimensionless unsteady boundary-region equations in the form given in [16], but now including the x, t derivatives:

$$2xU_x + 2U = \Phi_\eta + \Psi_\zeta\,, \tag{4a}$$

$$\Theta = \Psi_\eta - \Phi_\zeta\,, \tag{4b}$$

$$\nabla^2 U = 2xUU_x - \Phi U_\eta - \Psi U_\zeta + 2xU_t\,, \tag{4c}$$

$$\nabla^2 \Theta = 2x \left(U_\eta \Psi_x - U_\zeta \Phi_x + U\Theta_x - \Theta U_x \right)$$
$$+2 \left(\zeta UU_\eta - \eta UU_\zeta \right) - \Phi\Theta_\eta - \Psi\Theta_\zeta - 2U\Theta + 2x\Theta_t\,, \tag{4d}$$

where

$$\nabla^2 \equiv \frac{\partial^2}{\partial \eta^2} + \frac{\partial^2}{\partial \zeta^2}\,. \tag{4e}$$

As a streak generation mechanism, we allow for $O(Re^{-1/2})$ injection through the $\eta = 0$ boundary, leading to the boundary conditions

$$U = \Psi = 0\,, \quad \Phi = \Phi_{inj}(x, \zeta, t)\,, \quad \text{on} \quad \eta = 0\,, \tag{5a}$$

$$U \to 1, \quad \Psi \to 0, \quad \text{as} \quad \eta \to \infty, \tag{5b}$$

where Φ_{inj} defines an injection distribution on the plate surface. This localised injection is used to drive a steady streak base state for a subsequent linear stability analysis.

The far-field behaviour of (4) is analysed in detail in the work of Hewitt et al. [16]. Of particular note here is that

$$(\Phi, \Psi) \sim \frac{A(x,t)}{\zeta^2+\eta^2}(\eta, \zeta), \quad \text{for} \quad \zeta^2+\eta^2 \gg 1 \tag{6}$$

away from the boundary, leading to algebraic decay into the free stream of the cross-sectional (V, W) velocities, although the vorticity component defined by Θ in (4b) still decays exponentially. For the solutions presented herein, we enforce this algebraic behaviour explicitly to improve accuracy of solutions computed on a truncated domain, which turns out to be vitally important for numerical accuracy.

From the definition (2), this boundary injection Φ_{inj} corresponds to a weak dimensional injection velocity evaluated at the wall of

$$v^*(y^*=0) = -U^*_\infty Re^{-\frac{1}{2}}(2x)^{-\frac{1}{2}}\,\Phi_{inj}(x,\zeta,t). \tag{7}$$

Our focus is on injections ($\Phi_{inj} < 0$) that are localised in space with $|\Phi_{inj}| \to 0$ exponentially away from the injection region.

2. Non-parallel injection-driven steady streaks

Before we address the stability properties, we first consider a class of steady non-parallel developing base states; for this we extend the recent approach of Hewitt et al. [9]. The downstream evolution of the steady flow can be determined by decomposing the solution into a two-dimensional Blasius base flow plus a (short-spanwise scale) finite-amplitude correction:

$$U = U_B(\eta) + \tilde{U}(x,\eta,\zeta), \tag{8a}$$

$$\Phi = \Phi_B(\eta) + \tilde{\Phi}(x,\eta,\zeta), \tag{8b}$$

$$\Psi = \zeta\Psi_B(\eta) + \tilde{\Psi}(x,\eta,\zeta), \tag{8c}$$

$$\Theta = \zeta\Theta_B(\eta) + \tilde{\Theta}(x,\eta,\zeta). \tag{8d}$$

In this approach, zero injection ($\Phi_{inj} \equiv 0$) leads to the (two dimensional) Blasius state (denoted by the subscript-B terms) being the only non-zero contribution. For $\Phi_{inj} \neq 0$ this decomposition yields a nonlinear system of equations that must be marched numerically (parabolically) downstream in x from the leading edge for the flow quantities $(\tilde{U}, \tilde{\Phi}, \tilde{\Psi}, \tilde{\Theta})$.

We choose to induce a steady streak by a localised injection of the form

$$\Phi_{inj}(x,\zeta) = -\kappa F(x;x_0)G(\zeta), \tag{9a}$$

where

$$F(x;x_0) = e^{-\gamma(x-x_0)^2} \text{ and } G(\zeta) = e^{-C\zeta^2}(1-2C\zeta^2); \tag{9b}$$

in what follows we fix $\gamma = 10$ as variations of γ are equivalent to a rescaling of x, x_0. This is largely a Gaussian injection profile in both the downstream and spanwise coordinate, with a minor modification of the $(1-2C\zeta^2)$ factor, which ensures a zero net mass flux into the boundary layer. The magnitude of the injection is determined by κ, the downstream location of the injection is centred at $x = x_0$, whilst the (spanwise) lengthscale of the injection region decreases for increasing values of the constant C. This choice of injection is consistent with the recent paper of Hewitt et al. [9], but our focus is now instead on the stability properties of the resulting steady structures.

The baseflow evolution is determined by discretisation of (4) in the (ζ, η) plane, using a second-order central finite-difference scheme. The discretisation is over a uniform mesh in a transformed (computational) coordinate system, leading to a non-uniform mesh in the (ζ, η) plane. The downstream evolution is determined by Newton iteration applied at each downstream x location, using a routine Crank–Nicolson method for the downstream derivatives. This results in a mesh of $N_\zeta \times N_\eta$ nodal points and a $(4N_\zeta N_\eta \times 4N_\zeta N_\eta)$ sparse matrix inversion for each Newton iteration, which is handled via a multifrontal solver (MUMPS) [27]. Results were confirmed using a range of domain truncations and spatial steps, with typical values for moderate injection values being $N_\zeta = N_\eta = 401$ for $(\zeta, \eta) \in [0,20]\times[0,20]$, whilst a typical downstream spatial step was $\delta x = 0.005$.

In Fig. 1 we show contours of downstream velocity U in the cross sectional (ζ, η) plane for $\kappa = 12$, $x_0 = 10$. The contours are shown both near the injection location $x = 11$ (left column) and further downstream at $x = 14$ (right column). Variations in the width of the injection region (via $C = 0.1, 0.05, 0.025$) are shown from top to bottom in the figure. The steady injection (9) was shown by Hewitt & Duck [9] to be a good quantitative approximation of the steady streak experiments of [7] over a broad range of downstream positions. We therefore apply (9) as a convenient computational proxy to such experimentally-observed localised streaks. Data for an experimentally obtained base flow from [7] are also shown in Fig. 1(a) and we will return to discuss our results in this experimental context in Section 4.

3. Linear stability of a localised-streak

Our ultimate goal is to determine the stability of such steady streak states to linearised unsteady (time harmonic) perturbations, which result in downstream propagating, spatially developing waves. We tackle this problem via a combination of parabolic marching of the linearised disturbance equations, together with a local eigenvalue analysis in the context of the boundary-region formulation (4).

For base flows such as those shown in Fig. 1, driven by injection profiles described above in (9), we consider the linear stability to perturbations of a set forcing frequency ω (a real constant) via a decomposition into

$$U = [U_B(\eta) + \tilde{U}(x,\eta,\zeta)] + \epsilon e^{-i\omega t}u(x,\eta,\zeta) + \text{c.c.}, \tag{10a}$$

$$\Phi = [\Phi_B(\eta) + \tilde{\Phi}(x,\eta,\zeta)] + \epsilon e^{-i\omega t}\phi(x,\eta,\zeta) + \text{c.c.}, \tag{10b}$$

$$\Psi = [\zeta\Psi_B(\eta) + \tilde{\Psi}(x,\eta,\zeta)] + \epsilon e^{-i\omega t}\psi(x,\eta,\zeta) + \text{c.c.}, \tag{10c}$$

$$\Theta = [\zeta\Theta_B(\eta) + \tilde{\Theta}(x,\eta,\zeta)] + \epsilon e^{-i\omega t}\theta(x,\eta,\zeta) + \text{c.c.}. \tag{10d}$$

For each component the square-bracketed terms determine the localised, nonlinear, non-parallel streak of (8), whilst the $O(\epsilon)$ terms are the time-harmonic spatially developing linear disturbance field. The base flows are such that $\tilde{U}$ is symmetric about the centreline $\zeta = 0$, but the disturbance field can either be varicose (with u symmetric) or sinuous (with u antisymmetric).

To determine the downstream evolution of the $O(\epsilon)$ perturbation, we take two approaches. First we specify a form of initial forcing, via a small scale harmonic injection superimposed onto (9), and numerically (parabolically) march (u, ϕ, ψ, θ) downstream in tandem with the spatially developing base flow. Secondly, we address the stability locally as a bi-global eigenvalue calculation; the results from the two approaches will be compared.

3.1. Parabolic disturbance equations

On writing $u(x,\eta,\zeta) = f(x,\eta,\zeta)/x$, the linearised ($\epsilon \ll 1$) perturbation equations arise from substitution of (10) into (4):

$$2f_x = \phi_\eta + \psi_\zeta, \tag{11a}$$

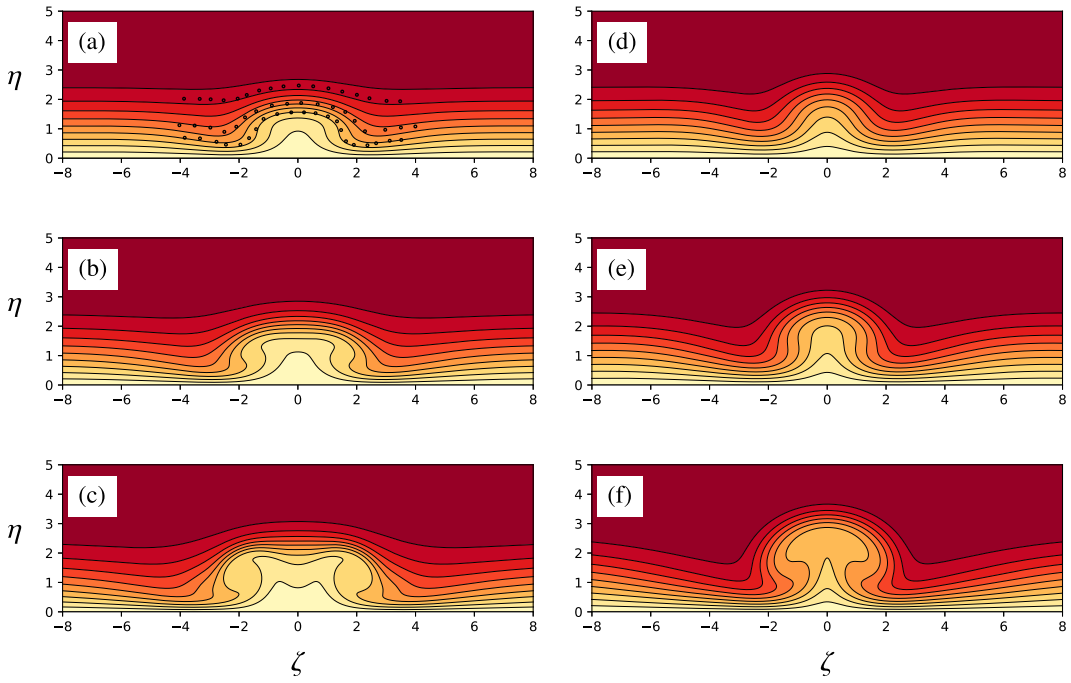

Fig. 1. Examples of the steady developing localised streak baseflow, as measured by the downstream velocity U. The streak is induced by injection at $x_0 = 10$, with an injection parameter of $\kappa = 12$. Two different downstream locations are shown, (a–c) at $x = 11$ and (d–f) further downstream at $x = 14$. The spanwise width of the injection slot increases from top to bottom, with (a,d) $C = 0.1$, (b,e) $C = 0.05$ and (c,f) $C = 0.025$. The contours are shown at $U = 0.1, 0.2, \ldots, 0.9$. Data points in (a) are experimental results for $U = 0.3, 0.5, 0.8$, as shown in Fig. 3(b) of [7].

$$\theta = \psi_\eta - \phi_\zeta \,, \tag{11b}$$

$$\begin{aligned} &x^{-1}\left\{\nabla^2 f + (\Phi_B + \tilde{\Phi})f_\eta + (\zeta\Psi_B + \tilde{\Psi})f_\zeta + 2(U_B + \tilde{U})f\right\} \\ &\quad + \phi(U_B' + \tilde{U}_\eta) + \psi\tilde{U}_\zeta \\ &\quad = 2(U_B + \tilde{U})f_x + 2f\tilde{U}_x - 2i\omega f \,, \end{aligned} \tag{11c}$$

$$\begin{aligned} &x^{-1}\left\{\nabla^2\theta + (\Phi_B + \tilde{\Phi})\theta_\eta + \phi(\tilde{\Theta}_\eta + \zeta\Theta_B') + \psi(\Theta_B + \tilde{\Theta}_\zeta)\right. \\ &\quad \left. + \theta_\zeta(\tilde{\Psi} + \Psi_B) + 2(U_B + \tilde{U})\theta\right\} \\ &-2x^{-2}\left(\zeta(U_B + \tilde{U})f_\eta + \zeta f(\tilde{U}_\eta + U_B') - \eta(U_B + \tilde{U})f_\zeta - \eta f\tilde{U}_\zeta\right) \\ &= 2\left((U_B' + \tilde{U}_\eta)\psi_x - \tilde{U}_\zeta\phi_x + (U_B + \tilde{U})\theta_x - x^{-1}(\zeta\Theta_B + \tilde{\Theta})f_x\right) \\ &+2\left(x^{-1}(f_\eta\tilde{\Psi}_x - f_\zeta\tilde{\Phi}_x + f\tilde{\Theta}_x) - \theta\tilde{U}_x\right) - 2i\omega\theta \,. \end{aligned} \tag{11d}$$

This system fully captures the spatial development of a perturbation, provided that the disturbance exists on the same length scales as the underlying localised streak. Computational results require (parabolic) marching of (11) in addition to the steady nonlinear streak flow, in x from suitable initial conditions. This is achieved by applying the same second-order Crank–Nicolson method as for the base flow. At each downstream position this marching procedure provides the full disturbance field in the cross-sectional (η, ζ) plane, which is equivalent to the (y^*, z^*) plane via the rescaling (1).

To excite the varicose mode we impose the same injection profile for the harmonic perturbation, as given in (9), via

$$\phi(x, \zeta, \eta = 0) = F(x; x_0)G(\zeta) \,, \tag{12}$$

which corresponds to a linear amplitude modulation of the injection. To excite a sinuous mode we correspondingly impose

$$\phi(x, \zeta, \eta = 0) = F(x; x_0)\zeta e^{-C\zeta^2} \,. \tag{13}$$

Fig. 2 shows the evolution of varicose perturbations, as measured by the downstream velocity perturbation u evaluated at the centreline $\zeta = 0$. Shown are the development of two varicose perturbations determined for $C = 0.1$ and a wider injection region of $C = 0.05$ (both with $\kappa = 12$, $x_0 = 10$). It is clear that the streak induced by the wider injection region ($C = 0.05$) is substantially more unstable with growth evident even at $x = 20$, whilst the narrower injection region ($C = 0.1$) leads to a peak growth near $x = 14$. The linear response has been normalised such that $|u| = 1$ at $x = x_0$, and the perturbation is seen to be localised away from the boundary, centred around the displaced shear layer of the streak. Fig. 2 overlays the base flow speed U, via contours of $U = 0.25, 0.5$ and 0.75, with the disturbance mostly centred between the 0.5 and 0.75 contours, but moving to higher values of U as the downstream location x is increased.

In Fig. 3 we vary both the amplitude of injection κ and the width of the injection region c, then determine a measure of local growth rate σ to be

$$\sigma = \frac{1}{\mathcal{E}}\frac{\mathrm{d}\mathcal{E}}{\mathrm{d}x} \,, \quad \text{where} \quad \mathcal{E} = \left(\int_{\zeta=0}^{\zeta=\infty}\int_{\eta=0}^{\eta=\infty} uu^* \,\mathrm{d}\eta\,\mathrm{d}\zeta\right)^{\frac{1}{2}} \,, \tag{14}$$

where the asterisk indicates a complex conjugation. The downstream behaviour of σ is shown from $x = x_0 = 10$ to $x = 12$. For $\kappa = 12$ the response is (locally) unstable $\sigma > 0$ and becomes increasingly unstable as C decreases (a widening injection region). For the values of C covered, we find that the growth of unstable sinuous modes is greater than any unstable varicose modes. For the lower injection amplitude $\kappa = 8$ the streak starts to stabilise to varicose modes. Restabilisation to sinuous modes occurs at lower values of κ.

Fig. 4(a) shows the effect of variations in the excitation frequency ω. As we shall show later, at high frequency (or far downstream) the growth rate scales linearly with frequency, which leads to the collapse of the shown data for $\omega = 5, 10$. Fig. 4(b) similarly shows the influence of the excitation point moving further downstream (with values of $x_0 = 5, 10, 20$) demonstrating no qualitative change.

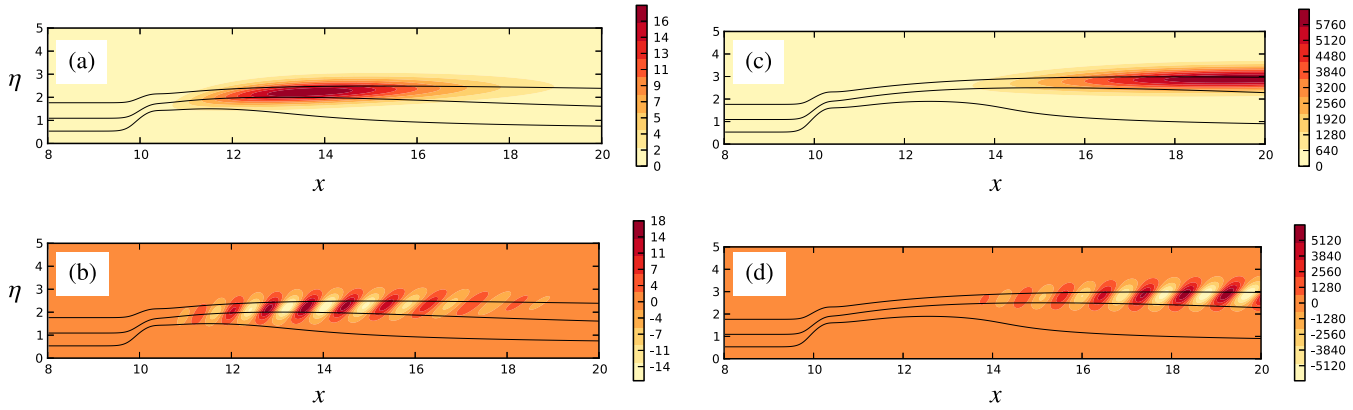

Fig. 2. The centreline $\zeta = 0$ evolution of a varicose linearised harmonic perturbation of frequency $\omega = 5$ for (a,b) $C = 0.1$ and (c,d) $C = 0.05$ for $\kappa = 12$ and $x_0 = 10$. Contours show the absolute value of the perturbation $u(x, \eta, \zeta = 0, \eta)$ in (a,c) and its real part in (b,d). In all cases the three contours shown as lines indicate where the steady baseflow satisfies $U(\zeta = 0, \eta) = 0.25, 0.5, 0.75$. The perturbation is normalised such that the peak value of $|u|$ is unity at $x = x_0$.

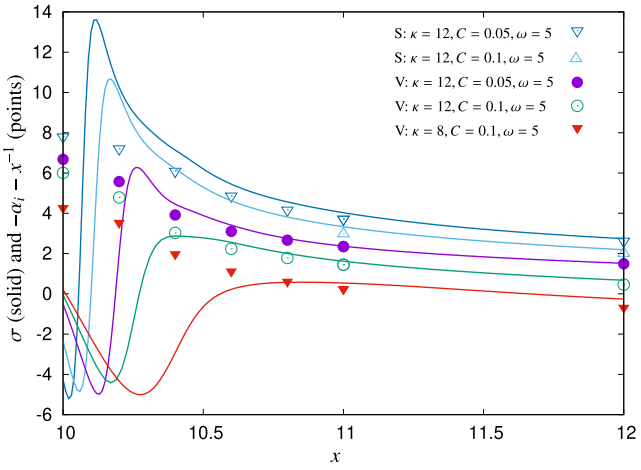

Fig. 3. Spatial growth rates (14) obtained by parabolic marching (solid) and the analogous local eigenvalues of (15) (points) for a range of disturbances and base flows, imposed at $x = x_0 = 10$. In the key, V denotes varicose modes, whilst S denotes sinuous modes.

3.2. Local stability analysis

On taking a weakly non-parallel approach to the disturbance equations (11) we can seek propagating wave solutions in the form

$$(u, \phi, \psi, \theta) = \left(x^{-1}\tilde{f}(\eta, \zeta; x), \tilde{\phi}(\eta, \zeta; x), \tilde{\psi}(\eta, \zeta; x), \tilde{\theta}(\eta, \zeta; x)\right) E\,, \tag{15a}$$

where

$$E = \exp\left\{i\left(\int^x \alpha(\xi)\,\mathrm{d}\xi\right)\right\}\,. \tag{15b}$$

At each downstream position, this approach results in a bi-global eigenvalue problem for $\alpha(x)$, but of course (whilst often effective) this is not fully justified asymptotically, apart from in the large-x or large-ω limit (as discussed below).

To determine the spectrum for α we apply the same non-uniformly distributed numerical mesh (as used for the base flow), with a second-order finite-difference scheme in ζ, η. This generates a (generalised) sparse matrix eigenvalue problem for $(\tilde{f}, \tilde{\phi}, \tilde{\psi}, \tilde{\theta})$ and α, associated to a given streak base flow (U, Φ, Ψ, Θ) as defined by (8). The matrix eigenvalue problem is tackled iteratively via a shift and invert method using the SLEPc library [28], to find the most dangerous spatial mode (the most negative value of α_i).

In Fig. 3 we compare the local prediction of the growth rate from the parabolic marching, as provided by (14) with the eigenvalue prediction for α. As seen from (15) there is a x^{-1} attenuation of the exponential growth in u and this is accounted for by comparing σ with $-\alpha_i - x^{-1}$. The disturbance is centred about $x = x_0 = 10$ and by $x = 11$ there is good quantitative agreement between the eigenvalue prediction and the parabolic marching results for $\omega = 5$.

Similar comparisons can be made for variations in the excitation frequency and excitation position, as shown by the data points in Fig. 4. As expected the agreement (at fixed x) is poorer at lower frequencies (Fig. 4a), although at fixed values of ω we expect the eigenvalues to provide improved quantitative predictions as x is increased. This can be observed by rescaling x in (15) in favour of a new coordinate downstream coordinate ωx.

Fig. 5 shows the (scaled) spatial growth rate obtained from the eigenvalue problem for a range of frequencies at $x = 11$, for the streak shown in Fig. 1(a). Both the varicose and sinuous modes are shown, with the sinuous being most unstable in this viscous problem. Further downstream at $x = 12$ Fig. 5(b) shows a reduction in the growth rate for both classes of disturbance symmetry, with a continued dominance of the sinuous mode.

The eigenfunctions associated with (15) are shown at $x = 11, 12$ in Fig. 6(a–b) (varicose) and 7(a–b) (sinuous) at $\omega = 5$. At these downstream positions, the eigenmodes are essentially indistinguishable from the distribution of u obtained by parabolic marching of (11), hence these are not shown.

3.3. Large-x inviscid (long-wave) stability

Sufficiently far downstream, on neglecting inverse powers of x in (11) we directly recover

$$2i\alpha\tilde{f} = \tilde{\phi}_\eta + \tilde{\psi}_\zeta\,, \tag{16a}$$

$$\tilde{\theta} = \tilde{\psi}_\eta - \tilde{\phi}_\zeta\,, \tag{16b}$$

$$\bar{U}_\eta\tilde{\phi} + \bar{U}_\zeta\tilde{\psi} = 2i\alpha(\bar{U} - \omega/\alpha)\tilde{f}\,, \tag{16c}$$

$$\bar{U}_\eta\tilde{\psi} - \bar{U}_\zeta\tilde{\phi} = -(\bar{U} - \omega/\alpha)\tilde{\theta}\,, \tag{16d}$$

where $\bar{U} = U_B + \tilde{U}$ is the downstream velocity distribution of the streak. In terms of a disturbance-wave pressure

$$p = \tilde{p}(\eta, \zeta; x)E + \text{c.c.}\,, \tag{16e}$$

the leading-order for large x satisfies

$$\tilde{p}_\eta = i\alpha(\bar{U} - \omega/\alpha)\tilde{\phi}\,, \tag{16f}$$

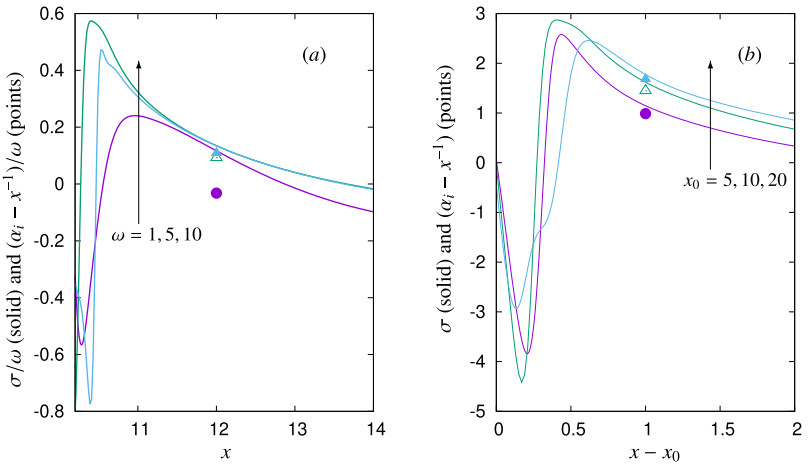

Fig. 4. (a) The local (varicose) growth rate (divided by ω) as defined by (14) for a range of excitation frequency $\omega = 1, 5, 10$ with $\kappa = 12$, $C = 0.1$, $x_0 = 10$ in (9). The growth rate scales linearly with ω at high frequency. (b) the growth rate obtained for an excitation frequency of $\omega = 5$, when $\kappa = 12$, $C = 0.1$ and $x_0 = 5, 10, 20$ in (9). In both (a,b) the data points show the local (eigenvalue) prediction of the growth rate provided by solution of the problem posed by (15).

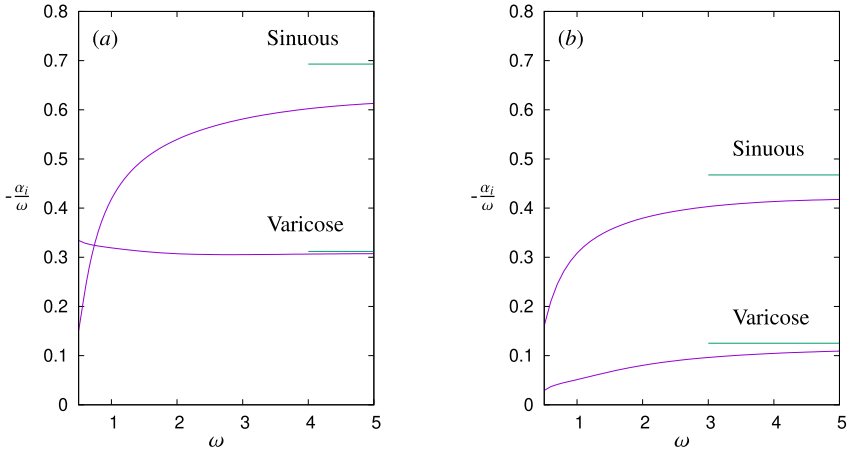

Fig. 5. Spatial growth rate predictions using the local bi-global eigenvalue problem defined by (15) with (a) $x = 11$ and (b) $x = 12$. In each case the asymptotic (long-wave Rayleigh) $x \gg 1$ prediction of (17) is shown as a straight line segment. Both figures are for a streak induced by (9) using $\kappa = 12$, $x_0 = 10$ and $C = 0.1$.

$$\tilde{p}_\zeta = i\alpha(\bar{U} - \omega/\alpha)\tilde{\psi}\,. \tag{16g}$$

From (16) we therefore recover the two-dimensional (long-wave limit of the) pressure Rayleigh equation

$$\nabla^2\tilde{p} = \frac{2}{\bar{U} - \omega/\alpha}\left(\tilde{p}_\eta\bar{U}_\eta + \tilde{p}_\zeta\bar{U}_\zeta\right)\,, \tag{17}$$

subject to

$$p \to 0 \quad \text{as} \quad \eta^2 + \zeta^2 \to \infty \tag{18}$$

as obtained in Hall & Horseman [29], Timoshin & Smith [30] and Hocking [31] for example, on setting a zero wavenumber.

The eigenvalue problem (17) is tackled using the same iterative sparse matrix formulation to determine the quantity ω/α, from which we can infer a value for α_i/ω. This value provides the asymptotic behaviour for (15) for increasing frequency or downstream position. Fig. 5 shows the predictions of (17) as the horizontal line segments, and these are approached as ω increases.

3.4. 'Upper-branch' modes

The previous eigenvalue problems rely on downstream wavelengths of the perturbation being sufficiently long compared to the local boundary-layer thickness. This assumption requires that $\omega \ll Re^{1/2}/(2x)^{1/2}$. At higher frequencies ω or (equivalently) when sufficiently far downstream ($x \gg 1$), the wavelength of the disturbance must eventually become comparable to the local boundary-layer thickness. In this limit we can formally recover an eigenvalue problem for the spatial growth rate via a parallel flow assumption applied in the usual manner, by inclusion of the corresponding shorter length scale (X) and faster time scale (T):

$$X = Re^{1/2}x\,, \quad T = Re^{1/2}t\,. \tag{19}$$

The harmonic behaviour of the waves is then

$$\exp\{i\,(\tilde{\alpha}X - \tilde{\omega}T)\}\,, \tag{20}$$

where $\tilde{\alpha} = (2x)^{-1/2}\bar{\alpha}$, $\tilde{\omega} = (2x)^{-1/2}\bar{\omega}$. The corresponding form of (17) is

$$(\nabla^2 - \bar{\alpha}^2)\tilde{p} = \frac{2}{\bar{U} - \bar{\omega}/\bar{\alpha}}\left(\tilde{p}_\eta\bar{U}_\eta + \tilde{p}_\zeta\bar{U}_\zeta\right)\,, \tag{21}$$

again subject to (18). This is the full Rayleigh pressure equation, see for example [29].

For fixed $\bar{\omega}$ (21) represents a challenging bi-global *polynomial* eigenvalue problem for the complex wavenumber $\bar{\alpha}$. Rather than dealing with this polynomial nature, we take an alternative approach. We solve (21) as a *nonlinear* problem for the unknowns of $\tilde{p}$ (at all nodal positions in the ζ–η plane) plus the complex value of $\bar{\alpha}$ via Newton iteration. To add $\bar{\alpha}$ as a single additional degree

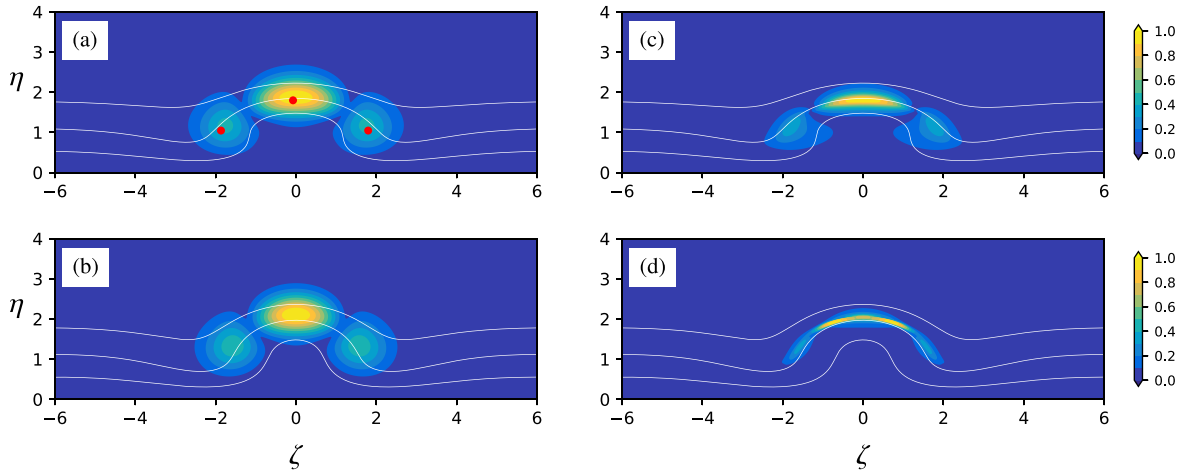

Fig. 6. Varicose eigenmodes showing the absolute value of the perturbation to the downstream flow velocity ($|u|$), as obtained from the local eigenvalue problem (15) with $\omega = 5$ at (a) $x = 11$ and (b) $x = 12$. Also shown are the corresponding inviscid eigenmodes with $\bar{\omega} = 0.45$ at (c) $x = 11$ and (d) $x = 12$. The eigenmodes are each normalised to a unit maximum, and each figure also shows contours of the downstream base flow velocity $U = 0.25, 0.5, 0.75$. The (red online) data points in (a) indicate maxima of experimentally obtained varicose eigenmodes at the same downstream position, as given in Fig. 7(a) of [7].

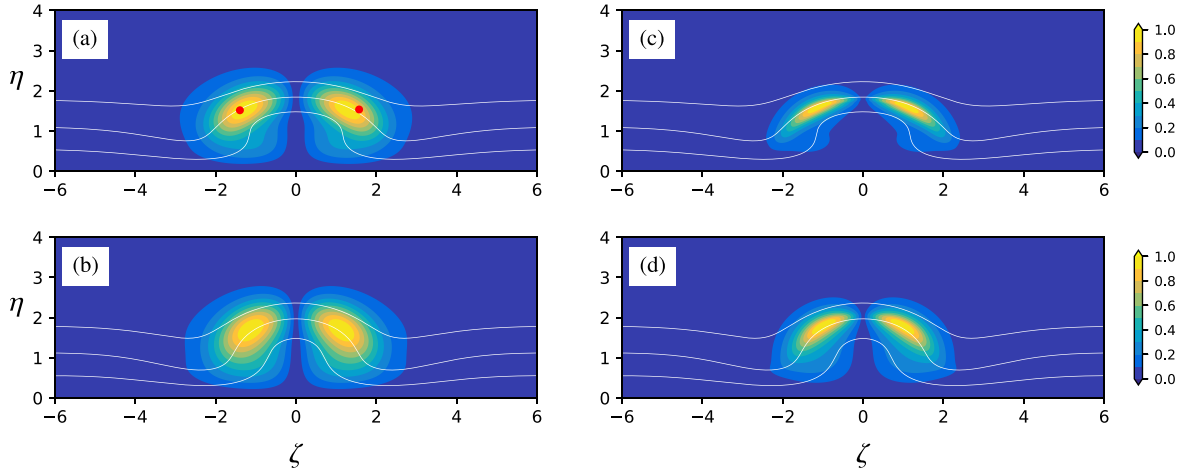

Fig. 7. Sinuous eigenmodes showing the absolute value of the perturbation to the downstream flow velocity ($|u|$), as obtained from the local eigenvalue problem (15) with $\omega = 5$ at (a) $x = 11$ and (b) $x = 12$. Also shown are the corresponding inviscid eigenmodes with $\bar{\omega} = 0.45$ at (c) $x = 11$ and (d) $x = 12$. The eigenmodes are each normalised to a unit maximum, and each figure also shows contours of the downstream base flow velocity $U = 0.25, 0.5, 0.75$. The (red online) data points in (a) indicate maxima of experimentally obtained sinuous eigenmodes at the same downstream position, as given in Fig. 7(b) of [7].

of freedom, we compensate by setting one of the pressure degrees of freedom to unity; thereby normalising the eigenmode. The advantage of this approach is that we avoid the polynomial nature of the eigenvalue problem, but this being an iterative method, we require a good initial guess and only recover one mode rather than a subset of the full spectrum. For the initial guess we use a long-wave eigenmode obtained from (17) at a small value of $\bar{\omega}$.

Fig. 8 shows the dependence of the most dangerous mode's growth rate $-\alpha_i$, as determined from (21) with $\kappa = 12$ ($x_0 = 10$, $C = 0.1$) over a range of ω at $x = 11$ and $x = 12$ for both the varicose and sinuous mode. We see behaviour that is in line with the experimental observations of Asai et al. [7], with a varicose instability providing a peak growth rate initially, but that the varicose mode rapidly becomes more stable as the streak develops/decays downstream. Further downstream the most unstable mode is sinuous, and this sinuous mode's growth rate is less sensitive to downstream position. We also see that the sinuous mode restabilises at a lower frequency than the varicose mode.

Examples of the inviscid eigenmode for u are shown in Fig. 6(c,d) for varicose modes and Fig. 7(c,d) for sinuous modes. As in the time-marched stability results of [13], and the experimental measurements of [7] the varicose mode peak near the maximum of transverse shear but there is no such simple correlation of the sinuous mode with the peak of spanwise shear. Both varicose and sinuous modes extend around the majority of the shear layer that is the streak boundary. A further comparison with experimental observations follows.

4. Experimental comparisons

The presence of comparable growth rates for both varicose and sinuous instabilities near to the source of a localised streak has been observed experimentally by Asai et al. [7] and it is worthwhile to consider how our current formulation applies to that configuration.

The experiments of Asai et al. [7] placed a 7.5 mm wide mesh screen 500 mm from the leading edge of a thin plate, in a uniform freestream flow of 4m/s. The height of the screen was 2.4 mm, which was also the displacement thickness of the corresponding (undisturbed) Blasius boundary layer at $x^* = 500$mm. As a result of the nonlinear perturbation caused by the mesh screen to the otherwise two-dimensional (Blasius) flow, an isolated streak develops downstream. This streak has an aspect ratio of $O(1)$

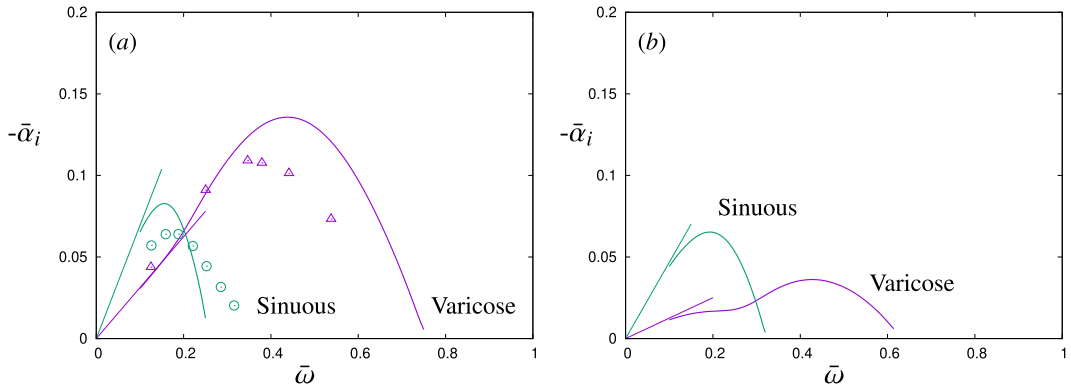

Fig. 8. Spatial growth rates obtained from solution of the inviscid equation (21) for a streak baseflow driven by $\kappa = 12$, $C = 0.1$ and $x_0 = 10$ in (9) evaluated at (a) $x = 11$ and (b) $x = 12$. In each case the long wave $\bar{\omega} \ll 1$ asymptote is shown as a straight line segment. Data points in (a) are the observed (non-dimensionalised) growth rates presented in [7], at $x^* = 550$mm, as discussed in Section 4.

in the cross sectional plane, matching the scalings of (1). The stability of the streak is then examined by localised harmonic (acoustic) excitation at $x^* \approx 510 - 515$mm.

Although no systematic study was undertaken in [9], quantitative agreement between the [7] experimental data for a steady streak has been obtained along the centreline ($z^* = 0$) over a range of $x^* = 550$ to 700 mm with parameter values of $\kappa = 12$, $\gamma = 10$, $C = 1/10$ and $x_0 = 10$ in (9). We therefore take this streak base flow as an approximation of the experimental configuration [7] and determine its (spatial) stability properties. A similar approach was taken in the DNS work of [13], by choosing a suitable body force term to represent the experimentally obtained streak flow data.

For $x_0 = 10$, to relate the dimensionless problem herein to the experimental configuration requires $L^* = 50$mm, leading to a global Reynolds number of $Re = 13{,}542$. Given this Reynolds number, the dimensional cross sectional coordinates are

$$(y^*, z^*) = L^* Re^{-1/2} (2x)^{1/2} (\eta, \zeta) \approx 2(\eta, \zeta)\,\text{mm}, \tag{22}$$

at $x^* = 550$ mm ($x = 11$). Apart from a dimensional factor of 2mm, the cross sectional results for $C = 0.1$ and $\kappa = 12$ in Fig. 1(a,d), 6 and 7 can be directly compared with the experimental data of [7].

The contours of the eigenmode component $|u|$ for this streak base flow are shown in Fig. 6(a,c) (varicose) and Fig. 7(a–c) (sinuous) at $x = 11$. The eigenmode shape is relatively insensitive to frequency over a broad range and (for a qualitative comparison) we also show the dimensionless position of the maxima of $|u|$ for the experimental data of [7] as obtained at ($x^* = 550$ mm, $x = 11$) with 110 Hz (varicose) and 60 Hz (sinuous) forcing.

A more sensitive comparison can be made of the spatial growth rates observed at $x^* = 550$mm in Figs. 11 and 13 of [7] to either the viscous prediction of Fig. 5 or the inviscid results of Fig. 8. The data of [7], for the baseflow of Fig. 1(a), are shown in Fig. 8.

The lowest excitation frequency in the experimental results is 40 Hz. This yields a value of $\omega = \pi$ in (15), and $\omega(2x/Re)^{1/2} \approx 0.127$ suggesting we are potentially in the viscous response regime . The relevant viscous prediction is given by Fig. 5, which gives a growth rate of 0.019 mm^{-1} for the varicose mode. The measured experimental value is 0.022 mm^{-1}.

The peak varicose growth rate in the experimental configuration is at 110 Hz, with $\omega(2x/Re)^{1/2} \approx 0.35$. This is in the inviscid regime of Fig. 8 with a predicted growth rate of 0.062 mm^{-1} compared to the observed value of 0.055 mm^{-1}. The peak predicted value for an inviscid varicose mode in Fig. 8 corresponds to a dimensional frequency of nearer 140 Hz, with a value of 0.067 mm^{-1}. Similarly, the sinuous modes at $x^* = 550$mm as reported by [7] give a peak growth rate of approximately 0.032 mm^{-1} at 50 Hz. The prediction of Fig. 8 translates to a peak dimensional growth rate at 50 Hz of 0.041 mm^{-1}.

5. Discussion

Isolated steady low-speed streaks in a Blasius boundary layer can be captured by a parabolised (and asymptotically-rigorous) form of the Navier–Stokes equations obtained in the high Reynolds number limit (the 'boundary-region equations'). Being parabolic in x, this governing system is an efficient method of obtaining fully nonlinear, non-parallel streaks in an otherwise two-dimensional developing layer, and are in essence the Görtler vortex equations applied to a localised structure with no curvature. Whilst there is some similarity in the governing system with that of the *Parabolised Navier–Stokes Equations* [32], there are also some important differences. Although the latter have proved to be a popular tool, especially to the aerospace community (being considerably faster computationally than DNS computations), their basic formulation is not asymptotically rigorous, and this is reflected in the need for ad-hoc restrictions in the choice of numerical parameters.

We focus attention on streaks that are driven by localised injection (but with zero net mass flux), and hence the streak decays downstream, with the far-downstream flow returning to a Blasius profile. The (steady) downstream evolution of a streak has been addressed previously in [9]. This work shows that the same governing equations in their unsteady form (4) can also be used to formulate parabolic linearised perturbation equations (11) which can be computed in tandem with the (streak) base flow. Downstream of a (temporally) periodic disturbance generator, we obtain 'transient' growth of perturbations prior to their ultimate decay as the streak amplitude itself decreases. We also formulate a weakly non-parallel eigenvalue approach to the spatial stability (15) of the streak, again based on the same boundary-region formulation and demonstrate consistency with the spatially marched evolution of a perturbation sufficiently far from the disturbance generator.

As the frequency of any (linear) disturbance generator increases, or equivalently if a disturbance is followed sufficiently far downstream, we pass through a long-wavelength Rayleigh region (17), and yet further downstream, we ultimately recover the full pressure Rayleigh equation for the disturbance (21).

For the streaks examined herein, the sinuous modes are always more dangerous for sufficiently long downstream wavelengths. However, as the frequency of excitation increases, in the Rayleigh regime, we find that varicose modes can dominate

the response near the injection region centred at $x = x_0$. However, the peak growth rate of the inviscid varicose mode decays more rapidly downstream and again the sinuous mode eventually dominates; this is clearly seen in Fig. 8.

We conclude that isolated streak flows are well captured by the system (4) and allow for effective predictions of both the steady streak and its spatial instability. The parabolic nature of (4) in the associated $Re \gg 1$ limit allows for an efficient computation of the streak/stability flow features. Despite the ad-hoc modelling of the experimental streak generation mechanism as a localised injection, the quantitative predictions have a good level of consistency with observations. In addition we also recover the qualitative features of (i) dominance of a varicose mode near $x = x_0$, (ii) more rapid decay of the varicose instability for increasing $x - x_0$ and a changeover to sinuous modes as the most unstable and (iii) restabilisation of the sinuous mode at a lower frequency than the varicose mode.

References

[1] J.-C. Loiseau, J.-C. Robinet, S. Cherubini, E. Leriche, Investigation of the roughness-induced transition: global stability analyses and direct numerical simulations, J. Fluid Mech. 760 (2014) 175–211.

[2] M.A. Bucci, D.K. Puckert, C. Andriano, J.-C. Loiseau, S. Cherubini, J.-C. Robinet, U. Rist, Roughness-induced transition by quasi-resonance of a varicose global mode, J. Fluid Mech. 836 (2018) 167–191.

[3] V. Citro, F. Giannetti, P. Luchini, F. Auteri, Global stability and sensitivity analysis of boundary-layer flows past a hemispherical roughness element, Phys. Fluids 27 (8) (2015) 084110.

[4] P.S. Klebanoff, W.G. Cleveland, K.D. Tidstrom, On the evolution of a turbulent boundary layer induced by a three-dimensional roughness element, J. Fluid Mech. 237 (1992) 101–187.

[5] N. Gregory, W.S. Walker, The effect of transition of isolated surface excrescences in the boundary layer, Tech. Rep. R. M. 2779 (1955).

[6] N. De Tullio, P. Paredes, N.D. Sandham, V. Theofilis, Laminar–turbulent transition induced by a discrete roughness element in a supersonic boundary layer, J. Fluid Mech. 735 (2013) 613–646.

[7] M. Asai, M. Minagawa, M. Nishioka, The instability and breakdown of a near-wall low-speed streak, J. Fluid Mech. 455 (2002) 289–314.

[8] R.D. Joslin, C.E. Grosch, Growth characteristics downstream of a shallow bump: Computation and experiment, Phys. Fluids 7 (12) (1995) 3042–3047.

[9] R.E. Hewitt, P.W. Duck, Localised streak solutions for a Blasius boundary layer, J. Fluid Mech. 849 (2018) 885–901.

[10] C. Cossu, L. Brandt, On Tollmien–Schlichting-like waves in streaky boundary layers, Eur. J. Mech. B Fluids 23 (6) (2004) 815–833.

[11] J.H.M. Fransson, L. Brandt, A. Talamelli, C. Cossu, Experimental study of the stabilization of Tollmien–Schlichting waves by finite amplitude streaks, Phys. Fluids 17 (5) (2005) 054110.

[12] L.L. Van Dommelen, R. Yapalparvi, Laminar boundary-layer separation control by Görtler-scale blowing, Eur. J. Mech. B Fluids 46 (2014) 1–16.

[13] L. Brandt, Numerical studies of the instability and breakdown of a boundary-layer low-speed streak, Eur. J. Mech. B Fluids 26 (1) (2007) 64–82.

[14] E. Piot, G. Casalis, U. Rist, Stability of the laminar boundary layer flow encountering a row of roughness elements: biglobal stability approach and DNS, Eur. J. Mech. B Fluids 27 (6) (2008) 684–706.

[15] S. Cherubini, M.D. De Tullio, P. De Palma, G. Pascazio, Transient growth in the flow past a three-dimensional smooth roughness element, J. Fluid Mech. 724 (2013) 642–670.

[16] R.E. Hewitt, P.W. Duck, Three-dimensional boundary layers with short spanwise scales, J. Fluid Mech. 756 (2014) 452–469.

[17] S.N. Brown, K. Stewartson, On similarity solutions of the boundary-layer equations with algebraic decay, J. Fluid Mech. 23 (04) (1965) 673–687.

[18] R.E. Hewitt, P.W. Duck, S.R. Stow, Continua of states in boundary-layer flows, J. Fluid Mech. 468 (2002) 121–152.

[19] A.J. Williams, R.E. Hewitt, Micro-slot injection into a boundary layer driven by a favourable pressure gradient, J. Eng. Math. 107 (2017) 19–35.

[20] R.E. Hewitt, P.W. Duck, A.J. Williams, Injection into boundary layers: solutions beyond the classical form, J. Fluid Mech. 822 (2017) 617–639.

[21] M. Higuera, J.M. Vega, Modal description of internal optimal streaks, J. Fluid Mech. 626 (2009) 21–31.

[22] P. Hall, The nonlinear development of Görtler vortices in growing boundary layers, J. Fluid Mech. 193 (1988) 243–266.

[23] P. Luchini, Reynolds-number-independent instability of the boundary layer over a flat surface, J. Fluid Mech. 327 (1996) 101–116.

[24] P. Luchini, Reynolds-number-independent instability of the boundary layer over a flat surface: optimal perturbations, J. Fluid Mech. 404 (1) (2000) 289–309.

[25] P. Andersson, M. Berggren, D.S. Henningson, Optimal disturbances and bypass transition in boundary layers, Phys. Fluids 11 (1) (1999) 134–150.

[26] P. Hall, S. Sherwin, Streamwise vortices in shear flows: harbingers of transition and the skeleton of coherent structures, J. Fluid Mech. 661 (2010) 178–205.

[27] P.R. Amestoy, I.S. Duff, J. -Y L'Excellent, Multifrontal parallel distributed symmetric and unsymmetric solvers, Comp. Methods in Appl. Mech. Eng. 184 (2) (2000) 501–520.

[28] V. Hernandez, J.E. Roman, V. Vidal, SLEPc: A Scalable and flexible toolkit for the solution of eigenvalue problems, ACM Trans. Math. Software 31 (3) (2005) 351–362.

[29] P. Hall, N.J. Horseman, The linear inviscid secondary instability of longitudinal vortex structures in boundary layers, J. Fluid Mech. 232 (1991) 357–375.

[30] S.N. Timoshin, F.T. Smith, Singular modes in Rayleigh instability of three-dimensional streamwise-vortex flows, J. Fluid Mech. 333 (1997) 139–160.

[31] L.M. Hocking, Long wavelength disturbances to non-planar parallel flow, J. Fluid Mech. 31 (4) (1968) 625–634.

[32] T. Herbert, Parabolized stability equations, Ann. Rev. Fluid Mech. 29 (1) (1997) 245–283, http://dx.doi.org/10.1146/annurev.fluid.29.1.245.